

Ultralow-power photonic chip-based soliton frequency combs

Junqiu Liu,^{1,*} Arslan S. Raja,^{1,*} Maxim Karpov,¹ Bahareh Ghadiani,¹ Martin H. P. Pfeiffer,¹ Nils J. Engelsen,¹ Hairun Guo,¹ Michael Zervas,² and Tobias J. Kippenberg^{1,†}

¹*École Polytechnique Fédérale de Lausanne (EPFL), CH-1015 Lausanne, Switzerland*

²*LIGENEC SA, CH-1015 Lausanne, Switzerland*

(Dated: May 18, 2022)

The generation of dissipative Kerr solitons in optical microresonators has provided a route to compact frequency combs of high repetition rate, which are amenable to chip-scale integration and have already been employed for frequency synthesizers, ultrafast ranging, coherent telecommunications and dual-comb spectroscopy. A particularly promising platform is photonic chip-scale microresonators based on Si₃N₄, which can be integrated with on-chip lasers. Yet to date, soliton formation in such Si₃N₄ microresonators requires the use of external amplifiers, either due to low quality (Q) factors or facet coupling losses. Moreover, these problems are compounded by the difficulty in accessing soliton states. While additional amplifiers and single-sideband modulators may overcome these challenges, for fully integrated Kerr soliton combs that combine a laser and a Kerr microresonator on a single chip, it is essential to resolve these challenges, particularly the power requirements. Here, we demonstrate ultralow-power single soliton formation in Si₃N₄ microresonators exhibiting Q factors of 6.2×10^6 with 6.6 mW total input power (4.1 mW in the waveguide) for devices of 1 THz repetition rate, using the photonic Damascene reflow process. We also access single soliton states with simple laser tuning in eight consecutive resonances over 60 nm wavelength range. Moreover, we demonstrate single soliton formation at a record-low chip input power of 48.6 mW with a repetition rate of 88 GHz—the lowest achieved for an integrated Si₃N₄ soliton comb, allowing applications such as ultrafast ranging and coherent communications. Our results show the technological readiness of Si₃N₄ optical waveguides for future all-on-chip nonlinear photonic devices with ultralow operating power.

I. INTRODUCTION

Optical frequency combs^{1,2} have revolutionized time-keeping and metrology over the past decades, and have found a wide variety of applications³. First discovered more than a decade ago, microresonator-based Kerr frequency combs^{4,5} are providing a route to chip-scale optical frequency combs, with broad bandwidth and repetition rates in the GHz to THz domain. Such Kerr fre-

quency combs have been demonstrated in a wide variety of platforms, including CMOS compatible materials such as silicon nitride (Si₃N₄)^{6,7}, which allow full photonic integration. The demonstration of Kerr combs in the dissipative Kerr soliton (DKS) regime⁸ has unlocked their full potential, by allowing reliable access to fully coherent Kerr comb states, which can attain large bandwidth via soliton Cherenkov radiation^{9–11}. Such DKS-based combs have already been successfully applied in counting the cycles of light¹², coherent communication on the receiver and transmitter sides¹³, dual-comb spectroscopy^{14,15}, ultrafast optical ranging^{16,17}, astrophysical spectrometer calibration^{18,19}, and for creating a photonic integrated frequency synthesizer²⁰. These developments highlight the potential of chip-scale DKS combs for timing, metrology and spectroscopy, allowing unprecedentedly compact devices at low operating power, fully compatible with wafer-scale integration and suitable for operation in space²¹.

A particularly promising platform for photonic integrated DKS combs is Si₃N₄, a material that is CMOS compatible, and has a wide transparency window and material optical nonlinearity. Recent advances in fabrication have enabled access to the anomalous group velocity dispersion regime (GVD) with sufficient waveguide height²², and circumvented the problems associated with the high tensile stress of Si₃N₄ film²³. Although DKS has been directly generated from a diode laser in a silica microresonator coupled to a tapered fiber only recently²⁴, this has not been possible for integrated devices including Si₃N₄. Yet, there are remaining challenges in DKS formation in Si₃N₄ microresonators, related to: (i) The comparatively low quality (Q) factor which increases the threshold power of DKS formation, compared to e.g. crystalline and silica microresonators. (ii) Optical coupling losses from the laser to the chip device, resulting from the optical mode mismatch at chip facets. (iii) Stable access to DKS states may require the use of complex excitation techniques such as "power kicking"²⁵ or single-sideband modulators²⁰. The first two challenges are particularly problematic for future photonic integration, as they necessitate the use of high-power lasers. So far, for integrated Si₃N₄ microresonator devices, DKS formation with power lower than 100 mW has only been achieved in microresonators of 1 THz free spectral range (FSR)^{20,26,27}. Yet in these experiments input coupling loss still necessitated the use of additional amplifiers to reach the required power levels of several tens of milliwatt in the chip. Meanwhile, low Kerr comb initiation

power at milliwatt or even sub-milliwatt level has been demonstrated in Si_3N_4 microresonators of Q exceeding 10^7 ^{28,29}, but solitons have not been observed due to insufficient anomalous GVD. Consequently, DKS formation has been limited to wavelength regions where amplifiers are available.

Here we demonstrate that the newly developed variant of photonic Damascene process³⁰, the *photonic Damascene reflow* process³¹, can overcome the outlined challenges and significantly reduce the required pump power for DKS formation in Si_3N_4 microresonators. Using simple piezo tuning of the laser, we demonstrate single soliton formation in 1-THz-FSR Si_3N_4 microresonators with record-low input power of 6.6 mW at the chip input facet, enabled by the microresonator's high Q (intrinsic $Q_0 > 6.2 \times 10^6$) and the efficient light coupling to the chip device (fiber-chip-fiber transmission $> 40\%$). Using only a tunable diode laser without optical amplifiers, we generate single solitons in eight consecutive resonances over a bandwidth exceeding 60 nm. Moreover, we demonstrate single soliton in Si_3N_4 microresonators of $Q_0 > 8.2 \times 10^6$ at the lowest repetition rate to date of 88 GHz, with record-low power of only 48.6 mW at the chip input facet (30.3 mW in the bus waveguide). Such ultralow-power DKSs of < 100 GHz repetition rate can significantly simplify the recently demonstrated dual-comb ultrafast distance measurements¹⁶ and optical coherent communications¹³, which required Erbium-doped fiber amplifiers (EDFA) to amplify the input power to above 1 Watt. In addition, the DKS combs demonstrated here have shown great potential for future integrated microwave generator using low-repetition-rate DKSs, and chip-based frequency synthesizers²⁰ via integration of on-chip lasers, semiconductor optical amplifiers and nonlinear microresonators. DKS formation in wavelength regions where amplifiers are not readily available could unlock new applications such as optical coherent tomography (OCT) at $1.3 \mu\text{m}$ ³² and for sensing of toxic gases and greenhouse gases e.g. methane at $1.6 \mu\text{m}$ ³³.

II. SAMPLE FABRICATION

Here, we briefly describe our fabrication process of Si_3N_4 microresonator samples. The waveguide is patterned on photoresist on the silicon dioxide (SiO_2) substrate, using deep-UV (DUV) stepper lithography. The pattern is then transferred from the DUV photoresist to the SiO_2 substrate via reactive ion etching (RIE) using C_4F_8 , O_2 and helium. Before the Si_3N_4 deposition on the patterned substrate using low pressure chemical vapor deposition (LPCVD), we do a "preform reflow", where the substrate is annealed for 18 hours at 1523 K temperature in an oxygen atmosphere. Due to the high temperature and the SiO_2 surface tension, the sidewall roughness caused by the RIE on the SiO_2 preform is significantly reduced, which reduces the scattering loss and leads to an ultrasmooth waveguide side surface. This is the key

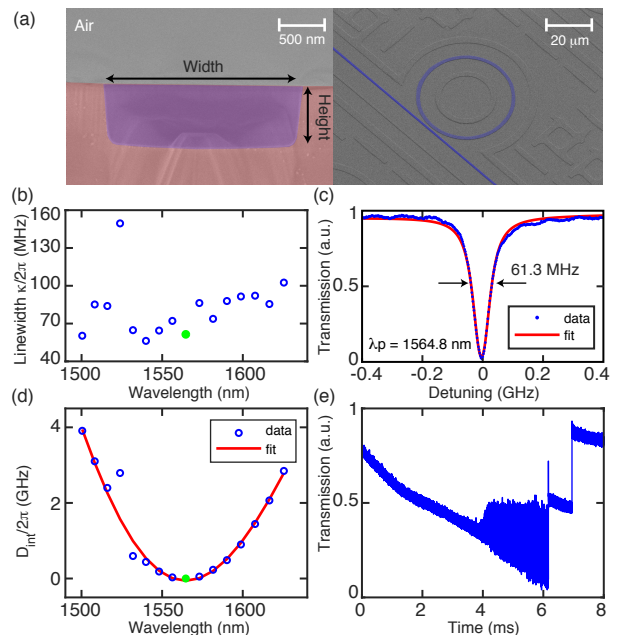


Figure 1. Device design and characterization of the 1-THz-FSR microresonators. (a) Left: Scanning electron microscope (SEM) image of the sample's cross-section. Si_3N_4 waveguide is blue shaded. SiO_2 bottom cladding is red shaded. Unshaded area is air. Right: SEM image of the tilted view of the sample. Si_3N_4 waveguide is blue shaded. (b) Measured linewidth versus wavelength of each resonance of the 1-THz-FSR microresonator's TE_{00} mode family. (c) The resonance at $\lambda_p = 1564.8$ nm and its fit, which is marked as a green solid circle in (b) and (d) and is the pump resonance for DKS formation in Fig. 2. This critically coupled resonance shows a total linewidth of 61.3 MHz, corresponding to an intrinsic loss $\kappa_0/2\pi \sim 30.7$ MHz and an intrinsic $Q_0 > 6.2 \times 10^6$. (d) Measured dispersion properties of the 1-THz-FSR microresonator's TE_{00} mode family. A strong mode crossing is observed around 1530 nm. (e) A soliton step longer than 1 ms is observed when the laser scans over the resonance from the blue-detuned side to the red-detuned side.

step resulting in the high Q of our Si_3N_4 microresonators with significantly reduced scattering loss.

The LPCVD Si_3N_4 film is deposited on the SiO_2 substrate, filling the preform trenches and defining the Si_3N_4 waveguides. The deposition is followed by chemical-mechanical polishing (CMP) which removes the excess Si_3N_4 and creates an ultrasmooth waveguide top surface. The substrate is annealed for another 3 hours, to drive out the residual hydrogen content introduced from the SiH_2Cl_2 and NH_3 utilized in the LPCVD Si_3N_4 process. No top SiO_2 cladding is deposited. Finally, the wafer is separated into chips by dicing or with deep RIE. Fig. 1(a) shows the SEM images of the final chip sample's cross-section and tilted top view. More details of fabrication process can be found in Ref.³⁰ and³¹.

For integrated chip-based nonlinear photonics, inverse nanotapers³⁴ are widely used as chip input couplers and can achieve high fiber-chip-fiber coupling efficiency and

broad operation bandwidth. The standard subtractive process^{28,35} requires the taper width to be less than 100 nm, to achieve fiber-chip-fiber coupling efficiency of 40% or more. Thus the resolution of stepper lithography is incompatible with the subtractive process, which requires instead electron beam lithography to pattern features of width below 100 nm. For our Damascene process, the required optimum taper width is above 400 nm, to attain 40% coupling efficiency, thus the stepper lithography is compatible with the Damascene process. The high coupling efficiency with much larger taper width, compared with the one used in the subtractive process, is due to the strong aspect-ratio-dependent RIE etch rate³⁶ of the preform RIE, which is specifically engineered and allows the creation of double-inverse nanotapers as chip input couplers³⁷. The double-inverse nanotaper enables high coupling efficiency (40% or more) with much larger taper width (above 400 nm) for both the transverse-electric (TE) and transverse-magnetic (TM) polarizations, due to the fact that the aspect-ratio-dependent RIE etch rate reduces the taper height, thus reducing the taper tip size, increasing the evanescent field size at the taper tip, and improving the mode match between the taper mode to the incident lensed fiber mode³⁷.

III. ULTRALOW-POWER SOLITON GENERATION OF 1 THZ REPETITION RATE

First, we present the results from 1-THz-FSR samples, with the fundamental TE mode of the microresonator (TE_{00}). The Si_3N_4 microresonators have a cross-section, width \times height, of $1.545 \times 0.750 \mu m^2$. The microresonator is critically coupled to a single mode bus waveguide, for high coupling ideality⁴⁰. The polarization of the incident light to the chip device is controlled by fiber polarization controllers, and the polarization state is measured using linear polarizers. The microresonator transmission trace is obtained from 1500 to 1630 nm using frequency-comb-assisted diode laser spectroscopy^{41,42}. The precise frequency of each data point is calibrated using a commercial femtosecond optical frequency comb with 250 MHz repetition rate. For the TE_{00} mode family, the FSR of the microresonator, the anomalous GVD and the linewidth of each resonance are extracted from the calibrated transmission trace. Fig. 1(b) shows the measured resonance linewidth versus wavelength. Fig. 1(c) shows the measured resonance at 1564.8 nm and the linewidth fit^{43,44}, which is pumped to generate DKS. This critically coupled resonance shows a total linewidth of $\kappa/2\pi = 61.3$ MHz, corresponding to an intrinsic loss $\kappa_0/2\pi \sim 30.7$ MHz and an intrinsic $Q_0 > 6.2 \times 10^6$.

Fig. 1(d) shows the measured microresonator integrated GVD, defined as $D_{int}(\mu) = \omega_\mu - \omega_0 - D_1\mu = D_2\mu^2/2 + D_3\mu^3/6 + \dots$ ⁴². Here ω_μ is the angular frequency of the μ -th resonance relative to the reference resonance $\omega_0 = 2\pi \cdot 191.7$ THz ($\lambda_p = 1564.8$ nm, as shown in Fig. 1(c)). $D_1/2\pi$ corresponds to the FSR. D_2 , D_3

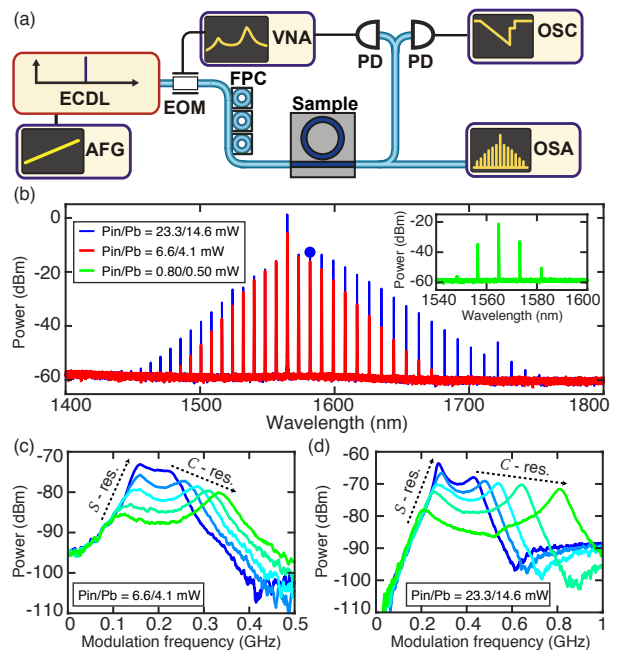


Figure 2. Ultralow-power comb initiation and single soliton formation in the 1-THz-FSR microresonator. (a) Experimental setup. ECDL: external-cavity diode laser. VNA: vector network analyzer. OSC: oscilloscope. OSA: optical spectrum analyzer. AFG: arbitrary function generator. FPC: fiber polarization controller. EOM: electro-optic modulator. PD: photodiode. Note the lack of an EDFA. (b) Ultralow-power comb initiation spectrum (green), single soliton spectrum with low laser power (red), and single soliton spectrum with high laser power (blue), pumped at $\lambda_p = 1564.8$ nm. The blue circle marks the maximum of the soliton spectral envelope, showing the Raman-induced soliton self-frequency shift³⁸. (c)-(d) Cavity response measurement using VNA³⁹, verifying that the two spectra shown in (b), red and blue, are both in a single soliton state. Each curve corresponds to a measurement with a pump detuning value to the cavity resonance. The evolution of the characteristic \mathcal{C} - and \mathcal{S} -resonances is shown for each state with increasing pump-cavity detuning.

and other higher order terms determine the profile of the GVD. For the 1-THz-FSR microresonator presented in Fig. 1, the fit values based on the measurement of ω_μ are $D_1/2\pi \sim 1024$ GHz, $D_2/2\pi \sim 123$ MHz and $D_3/2\pi \sim 4.0$ kHz.

When the pump laser scans over the resonance from the blue-detuned side to the red-detuned side, a step in the transmission spectrum is observed, as shown in Fig. 1(e), signaling to the DKS formation⁸. To generate and characterize DKSs, we use a setup as shown in Fig. 2(a). Note that no EDFA is used here. Fiber-chip-fiber transmission of 40% (coupling efficiency of 63% per device facet) is achieved via double-inverse nanotapers on the chip facets³⁷. The input power (P_{in}) is defined as the power measured before the input lensed fiber which couples light into the chip device. Thus the optical power

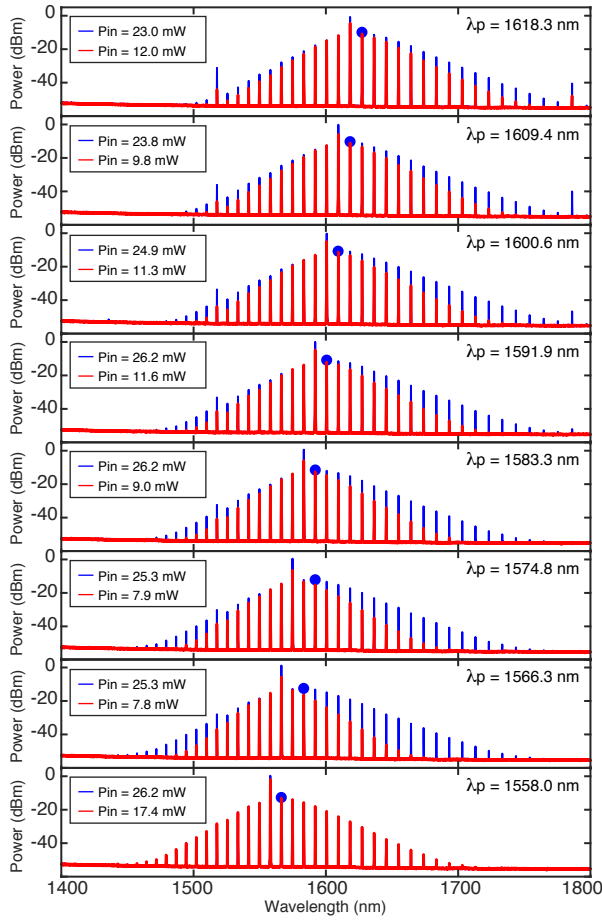


Figure 3. Single soliton formation in eight consecutive resonances over 60 nm range in another 1-THz-FSR microresonator. Single soliton spectra with low laser power (red) and high laser power (blue) are shown for eight consecutive resonances, pumped at different wavelength λ_p . Blue circles mark the maximum of soliton spectrum envelope, showing the Raman-induced soliton self-frequency shift.

in the bus waveguide (P_b) on the chip, which directly pumps the microresonator, is calculated as $P_b = 0.63P_{in}$.

We study the DKS spectra with varying optical input power P_{in} . As shown in Fig. 2(b), comb initiation is observed when P_{in} (P_b) reaches 800 (500) μ W. Due to the high GVD ($D_2/2\pi \sim 123$ MHz) and the low linewidth ($\kappa/2\pi = 61.3$ MHz), corresponding to $\sqrt{\kappa/D_2} < 1$, the first sidebands start oscillating in the resonance modes adjacent to the pump at $\lambda_p = 1564.8$ nm. As the DKS step length is longer than 1 ms, the single soliton state can be accessed with the simple forward tuning method⁸. A single soliton spectrum is observed, when P_{in} (P_b) reaches 6.6 (4.1) mW. The spectrum is further broadened with higher laser power, until the maximum power of the laser is reached at around 23 mW. At P_{in} (P_b) of 23.3 (14.6) mW, the single soliton shows a spectral bandwidth exceeding 300 nm, with a prominent Raman-induced soliton self-frequency shift³⁸. Fig. 2(c) and (d) show that, the two spectra with $P_{in} = 6.6$ mW and $P_{in} = 23.3$ mW

are indeed single soliton states, as verified by the system response measurement using vector network analyzer (VNA)³⁹. The observed double resonance response corresponds to the cavity resonance of the continuous wave ("C-resonance"), and the soliton-induced resonance ("S-resonance"). These two resonances can be clearly distinguished by increasing the detuning of the DKS state³⁹.

We next investigate the DKS formation over the full tuning range of the diode laser. Fig. 3 show the DKS formation in eight consecutive resonances, from 1558.0 to 1618.3 nm, in a different 1-THz-FSR microresonator. Two spectra are shown with each resonance: the red one shows the single soliton spectrum with low laser power, and the blue one with the maximum laser power allowed by our laser. The formation of DKSs in a broad range of resonances demonstrates the robustness and reliability of our photonic Damascene reflow process and offers extra flexibility to investigate spectrally localized effects, such as avoided mode crossings, which can enable the formation of dark pulses in the normal GVD region^{45,46}, and breathing solitons⁴⁷.

IV. ULTRALOW-POWER PHOTONIC CHIP-BASED SOLITON COMB OF <100 GHz REPETITION RATE

In the second part of our work, we demonstrate ultralow-power DKS formation in a 88-GHz-FSR microresonator. Fig. 4(a) shows the microscope image of the 88-GHz-FSR microresonators. Meander bus waveguides are used in order to densely pack a large number of devices on one chip. Here the main study is focused on the TE_{00} mode family. The Si_3N_4 microresonators have a cross-section, width \times height, of $1.575 \times 0.750 \mu m^2$, slightly larger than the ones used for 1-THz-FSR solitons. The measured linewidth of each TE_{00} resonance is shown in Fig. 4(d). These resonances are all under-coupled. Larger linewidths are found in the wavelength region from 1500 to 1550 nm, due the absorption by the nitrogen-hydrogen (N-H) and silicon-hydrogen (Si-H) bonds in LPCVD Si_3N_4 material^{48,49}. These bonds are introduced during typical LPCVD Si_3N_4 process based on SiH_2Cl_2 and NH_3 precursors⁵⁰, and can be only partially removed by thermal annealing. Fig. 4(b) shows the resonance at $\lambda_p = 1558.0$ nm. The resonance fit shows a loaded linewidth of $\kappa/2\pi = 30.3$ MHz, and the estimated intrinsic loss based on the resonance fit is $\kappa_0/2\pi \sim 23.3$ MHz, corresponding to the intrinsic $Q_0 > 8.2 \times 10^6$. Fig. 4(c) shows the resonance at $\lambda_p = 1620.0$ nm, with a loaded linewidth of $\kappa/2\pi = 28.7$ MHz, and the estimated intrinsic loss is $\kappa_0/2\pi \sim 17.3$ MHz, corresponding to the intrinsic $Q_0 > 10.7 \times 10^6$. Note that although the microresonator cross-sections are nearly identical, the measured Q_0 of the 88-GHz-FSR microresonator is higher than the Q_0 of 1-THz-FSR microresonator. This is likely due to the former's larger radius, which reduces the interaction of the optical mode

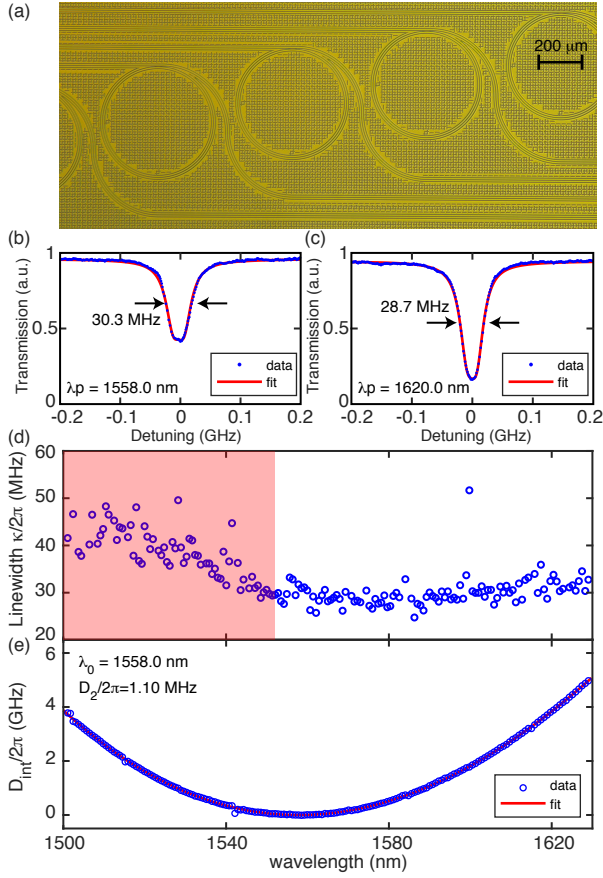


Figure 4. Dispersion and resonance linewidth characterization of the 88-GHz-FSR microresonator. (a) Microscope image of densely packed 88-GHz-FSR microresonators, using meander bus waveguides. (b) The pump resonance at $\lambda_p = 1558.0$ nm and its fit, with the loaded linewidth of $\kappa_0/2\pi = 30.3$ MHz and fitted intrinsic linewidth of $\kappa_0/2\pi \sim 23.2$ MHz, corresponding to $Q_0 > 8.2 \times 10^6$. (c) Measured linewidth versus wavelength of each resonance of the 88-GHz-FSR microresonator's TE_{00} mode family. Larger linewidths are found in the wavelength region from 1500 to 1550 nm (red shaded area), due to the absorption by the N-H and Si-H bonds in LPCVD Si_3N_4 . (d) Measured dispersion properties of the 88-GHz-FSR microresonator's TE_{00} mode family. Several avoided mode crossings are observed, however they are highly localized spectrally and thus only distort the dispersion of a few local resonances.

with the sidewall roughness. Fig. 4(e) shows the measured microresonator D_{int} with respect to the reference resonance $\omega_0 = 2\pi \cdot 192.6$ THz ($\lambda_p = 1558.0$ nm, as shown in Fig. 4(b)). The fit values obtained from the dispersion measurement are $D_1/2\pi \sim 88.63$ GHz, $D_2/2\pi \sim 1.10$ MHz and $D_3/2\pi \sim \mathcal{O}(1)$ kHz.

Larger optical powers are required for DKS formation in the 88-GHz-FSR microresonator, due to the decreased optical finesse compared to 1-THz-FSR microresonators. Therefore an EDFA is used to slightly amplify the optical power to $P_{in} = 48.6$ mW ($P_b = 30.6$ mW). To access the single soliton state, we use a single-sideband modulator²⁰ and a single soliton spectrum is observed as

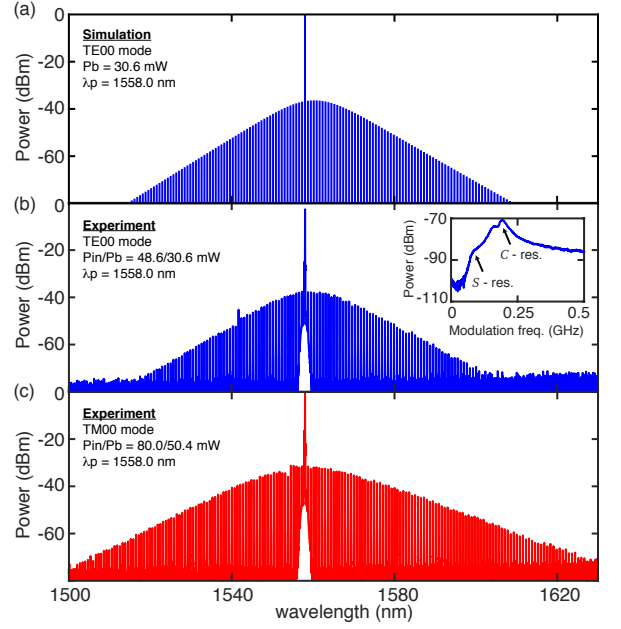


Figure 5. Ultralow-power single soliton formation in the 88-GHz-FSR microresonator. (a) Simulated single soliton spectrum based on the measured microresonator's parameters, in the TE_{00} mode. $P_b = 30.6$ mW corresponds to $P_{in} = 48.6$ mW. (b) Single soliton spectrum pumped at $\lambda_p = 1558.0$ nm in the TE_{00} mode, with a pump power of $P_{in} = 48.6$ mW ($P_b = 30.6$ mW). Inset: cavity response measurement using the VNA, verifying that the spectrum is a single soliton state. (c) Single soliton spectrum pumped at $\lambda_p = 1558.0$ nm in the TM_{00} mode, with the pump power $P_{in} = 80.0$ mW ($P_b = 50.4$ mW).

shown in Fig. 5(b), verified by a response measurement with the VNA. Fig. 5(a) shows the simulation of soliton formation based on Lugiato-Lefever equation⁵¹ using the measured microresonator parameters. The simulated soliton spectrum is nearly identical to the measured one. We also generate a single soliton in the TM_{00} mode ($D_1/2\pi \sim 86.35$ GHz, $D_2/2\pi \sim 0.967$ MHz, $D_3/2\pi \sim 5.4$ kHz) pumped at the wavelength $\lambda_p = 1558.0$, with the input power $P_{in} = 80.0$ mW ($P_b = 50.6$ mW), as shown in Fig. 5(c). This single soliton spectrum is broader than the one in the TE_{00} mode shown in Fig. 5(b), likely due to the higher power and lower D_2 value. This represents a significant power reduction, compared to prior work^{13,16} using DKSs in Si_3N_4 of repetition rate less than 100 GHz, where input power levels exceeding 2 watts were used.

V. CONCLUSION

In summary, we present ultralow-power single soliton formation in integrated high- Q Si_3N_4 microresonators. We demonstrate comb initiation at sub-milliwatt input power, single soliton formation at 6.6 mW input power, and eight single soliton spectra in eight consecutive res-

onances over 60 nm bandwidth, in 1-THz-FSR microresonators. Furthermore, we demonstrate soliton formation in a 88-GHz-FSR microresonator using 48.6 mW input power, a record-low value. The ultralow-power soliton formation results mainly from the microresonator's high Q (estimated intrinsic $Q_0 > 6.2 \times 10^6$ in the 1-THz-FSR microresonators and $Q_0 > 8.2 \times 10^6$ in the 88-GHz-FSR microresonator) and the $>40\%$ device-through coupling efficiency. Our work demonstrates the potential of ultralow-power DKS formation in Si_3N_4 integrated microresonators, central for applications such as integrated chip-based microwave generator using low repetition rate solitons, integrated frequency synthesizer, OCT and dual-comb spectroscopy.

Note added: During the preparation of this manuscript, ultralow-power DKS formation was demonstrated in Si_3N_4 microresonators integrated with an on-

chip laser⁵².

FUNDING INFORMATION

Defense Advanced Research Projects Agency (DARPA), Defense Sciences Office (DSO) (HR0011-15-C-0055); European Union's Horizon 2020 Framework Programme (H2020) (709249); Swiss National Science Foundation (SNSF) (161573); European Space Research and Technology Centre (4000116145/16/NL/MH/GM).

ACKNOWLEDGMENTS

The Si_3N_4 microresonator samples were fabricated in the EPFL center of MicroNanoTechnology (CMi). We acknowledge Tiago Morais for the assistance in sample fabrication.

-
- * J.L. and A.S.R. contributed equally to this work
[†] tobias.kippenberg@epfl.ch
- ¹ T. Udem, R. Holzwarth, and T. W. Hänsch, *Nature* **416**, 233 (2002).
 - ² S. T. Cundiff and J. Ye, *Rev. Mod. Phys.* **75**, 325 (2003).
 - ³ N. R. Newbury, *Nature Photonics* **5**, 186 (2011).
 - ⁴ P. Del'Haye, A. Schliesser, O. Arcizet, T. Wilken, R. Holzwarth, and T. J. Kippenberg, *Nature* **450**, 1214 (2007).
 - ⁵ T. J. Kippenberg, R. Holzwarth, and S. A. Diddams, *Science* **332**, 555 (2011).
 - ⁶ J. S. Levy, A. Gondarenko, M. A. Foster, A. C. Turner-Foster, A. L. Gaeta, and M. Lipson, *Nature Photonics* **4**, 37 (2010).
 - ⁷ D. J. Moss, R. Morandotti, A. L. Gaeta, and M. Lipson, *Nature Photonics* **7**, 597 (2013).
 - ⁸ T. Herr, V. Brasch, J. D. Jost, C. Y. Wang, N. M. Kondratiev, M. L. Gorodetsky, and T. J. Kippenberg, *Nature Photonics* **8**, 145 (2014).
 - ⁹ J. K. Jang, M. Erkintalo, S. G. Murdoch, and S. Coen, *Opt. Lett.* **39**, 5503 (2014).
 - ¹⁰ C. Milián and D. Skryabin, *Opt. Express* **22**, 3732 (2014).
 - ¹¹ V. Brasch, M. Geiselmann, T. Herr, G. Lihachev, M. H. P. Pfeiffer, M. L. Gorodetsky, and T. J. Kippenberg, *Science* **351**, 357 (2016).
 - ¹² J. D. Jost, T. Herr, C. Lecaplain, V. Brasch, M. H. P. Pfeiffer, and T. J. Kippenberg, *Optica* **2**, 706 (2015).
 - ¹³ P. Marin-Palomo, J. N. Kemal, M. Karpov, A. Kordts, J. Pfeifle, M. H. P. Pfeiffer, P. Trocha, S. Wolf, V. Brasch, M. H. Anderson, R. Rosenberger, K. Vijayan, W. Freude, T. J. Kippenberg, and C. Koos, *Nature* **546**, 274 (2017).
 - ¹⁴ M. Yu, Y. Okawachi, A. G. Griffith, N. Picqué, M. Lipson, and A. L. Gaeta, *arXiv* **1610.01121v2** (2016).
 - ¹⁵ M.-G. Suh, Q.-F. Yang, K. Y. Yang, X. Yi, and K. J. Vahala, *Science* **354**, 600 (2016).
 - ¹⁶ P. Trocha, M. Karpov, D. Ganin, M. H. P. Pfeiffer, A. Kordts, S. Wolf, J. Krockenberger, P. Marin-Palomo, C. Weimann, S. Randel, W. Freude, T. J. Kippenberg, and C. Koos, *Science* **359**, 887 (2018).
 - ¹⁷ M.-G. Suh and K. J. Vahala, *Science* **359**, 884 (2018).
 - ¹⁸ E. Obrzud, M. Rainer, A. Harutyunyan, M. Anderson, M. Geiselmann, B. Chazelas, S. Kundermann, S. Lecomte, M. Cecconi, A. Ghedina, E. Molinari, F. Pepe, F. Wildi, F. Bouchy, T. Kippenberg, and T. Herr, *arXiv* **1712.09526** (2017).
 - ¹⁹ M.-G. Suh, X. Yi, Y.-H. Lai, S. Leifer, I. S. Grudinin, G. Vasisht, E. C. Martin, M. P. Fitzgerald, G. Doppmann, J. Wang, D. Mawet, S. B. Papp, S. A. Diddams, C. Beichman, and K. Vahala, *arXiv* **1801.05174v1** (2017).
 - ²⁰ D. T. Spencer, T. Drake, T. C. Briles, J. Stone, L. C. Sinclair, C. Fredrick, Q. Li, D. Westly, B. R. Ilic, A. Bluestone, N. Volet, T. Komljenovic, L. Chang, S. H. Lee, D. Y. Oh, M.-G. Suh, K. Y. Yang, M. H. P. Pfeiffer, T. J. Kippenberg, E. Norberg, L. Theogarajan, K. Vahala, N. R. Newbury, K. Srinivasan, J. E. Bowers, S. A. Diddams, and S. B. Papp, *Nature* (2018), [10.1038/s41586-018-0065-7](https://doi.org/10.1038/s41586-018-0065-7).
 - ²¹ V. Brasch, Q.-F. Chen, S. Schiller, and T. J. Kippenberg, *Opt. Express* **22**, 30786 (2014).
 - ²² M. A. Foster, A. C. Turner, J. E. Sharping, B. S. Schmidt, M. Lipson, and A. L. Gaeta, *Nature* **441**, 960 (2006).
 - ²³ K. Luke, A. Dutt, C. B. Poitras, and M. Lipson, *Opt. Express* **21**, 22829 (2013).
 - ²⁴ N. Volet, X. Yi, Q. Yang, E. J. Stanton, P. A. Morton, K. Y. Yang, K. J. Vahala, and J. E. Bowers, *Laser Photonics Rev.* **0**, 1700307.
 - ²⁵ V. Brasch, M. Geiselmann, M. H. P. Pfeiffer, and T. J. Kippenberg, *Opt. Express* **24**, 29312 (2016).
 - ²⁶ Q. Li, T. C. Briles, D. A. Westly, T. E. Drake, J. R. Stone, B. R. Ilic, S. A. Diddams, S. B. Papp, and K. Srinivasan, *Optica* **4**, 193 (2017).
 - ²⁷ M. H. P. Pfeiffer, C. Herkommer, J. Liu, H. Guo, M. Karpov, E. Lucas, M. Zervas, and T. J. Kippenberg, *Optica* **4**, 684 (2017).
 - ²⁸ Y. Xuan, Y. Liu, L. T. Varghese, A. J. Metcalf, X. Xue, P.-H. Wang, K. Han, J. A. Jaramillo-Villegas, A. A. Noman, C. Wang, S. Kim, M. Teng, Y. J. Lee, B. Niu, L. Fan,

- J. Wang, D. E. Leaird, A. M. Weiner, and M. Qi, *Optica* **3**, 1171 (2016).
- ²⁹ X. Ji, F. A. S. Barbosa, S. P. Roberts, A. Dutt, J. Carnadas, Y. Okawachi, A. Bryant, A. L. Gaeta, and M. Lipson, *Optica* **4**, 619 (2017).
- ³⁰ M. H. P. Pfeiffer, A. Kordts, V. Brasch, M. Zervas, M. Geiselmann, J. D. Jost, and T. J. Kippenberg, *Optica* **3**, 20 (2016).
- ³¹ M. H. P. Pfeiffer, J. Liu, A. S. Raja, T. Morais, B. Ghadani, and T. J. Kippenberg, [arXiv 1802.08315v1](https://arxiv.org/abs/1802.08315v1) (2018).
- ³² S. H. Yun, G. J. Tearney, B. E. Bouma, B. H. Park, and J. F. de Boer, *Opt. Express* **11**, 3598 (2003).
- ³³ L. Tombez, E. J. Zhang, J. S. Orcutt, S. Kamlapurkar, and W. M. J. Green, *Optica* **4**, 1322 (2017).
- ³⁴ V. R. Almeida, R. R. Panepucci, and M. Lipson, *Opt. Lett.* **28**, 1302 (2003).
- ³⁵ A. Gondarenko, J. S. Levy, and M. Lipson, *Opt. Express* **17**, 11366 (2009).
- ³⁶ R. A. Gottscho, C. W. Jurgensen, and D. J. Vitkavage, *J. Vac. Sci. Technol. B* **10**, 2133 (1992).
- ³⁷ J. Liu, A. S. Raja, M. H. P. Pfeiffer, C. Herkommer, H. Guo, M. Zervas, M. Geiselmann, and T. J. Kippenberg, [arXiv 1803.02662v1](https://arxiv.org/abs/1803.02662v1) (2018).
- ³⁸ M. Karpov, H. Guo, A. Kordts, V. Brasch, M. H. P. Pfeiffer, M. Zervas, M. Geiselmann, and T. J. Kippenberg, *Phys. Rev. Lett.* **116**, 103902 (2016).
- ³⁹ H. Guo, M. Karpov, E. Lucas, A. Kordts, M. H. P. Pfeiffer, V. Brasch, G. Lihachev, V. E. Lobanov, M. L. Gorodetsky, and T. J. Kippenberg, *Nature Physics* **13**, 94 (2016).
- ⁴⁰ M. H. P. Pfeiffer, J. Liu, M. Geiselmann, and T. J. Kippenberg, *Phys. Rev. Applied* **7**, 024026 (2017).
- ⁴¹ P. Del’Haye, O. Arcizet, M. L. Gorodetsky, R. Holzwarth, and T. J. Kippenberg, *Nature Photonics* **3**, 529 (2009).
- ⁴² J. Liu, V. Brasch, M. H. P. Pfeiffer, A. Kordts, A. N. Kamel, H. Guo, M. Geiselmann, and T. J. Kippenberg, *Opt. Lett.* **41**, 3134 (2016).
- ⁴³ M. L. Gorodetsky, A. D. Pryamikov, and V. S. Ilchenko, *J. Opt. Soc. Am. B* **17**, 1051 (2000).
- ⁴⁴ Q. Li, A. A. Eftekhar, Z. Xia, and A. Adibi, *Phys. Rev. A* **88**, 033816 (2013).
- ⁴⁵ Y. Liu, Y. Xuan, X. Xue, P.-H. Wang, S. Chen, A. J. Metcalf, J. Wang, D. E. Leaird, M. Qi, and A. M. Weiner, *Optica* **1**, 137 (2014).
- ⁴⁶ X. Xue, Y. Xuan, Y. Liu, P.-H. Wang, S. Chen, J. Wang, D. E. Leaird, M. Qi, and A. M. Weiner, *Nature Photonics* **9**, 594 (2015).
- ⁴⁷ H. Guo, E. Lucas, M. H. P. Pfeiffer, M. Karpov, M. Anderson, J. Liu, M. Geiselmann, J. D. Jost, and T. J. Kippenberg, *Phys. Rev. X* **7**, 041055 (2017).
- ⁴⁸ S. C. Mao, S. H. Tao, Y. L. Xu, X. W. Sun, M. B. Yu, G. Q. Lo, and D. L. Kwong, *Opt. Express* **16**, 20809 (2008).
- ⁴⁹ J. F. Bauters, M. J. R. Heck, D. D. John, J. S. Barton, C. M. Bruinink, A. Leinse, R. G. Heideman, D. J. Blumenthal, and J. E. Bowers, *Opt. Express* **19**, 24090 (2011).
- ⁵⁰ J. Yota, J. Hander, and A. A. Saleh, *J. Vac. Sci. Technol. A* **18**, 372 (2000).
- ⁵¹ L. A. Lugiato and R. Lefever, *Phys. Rev. Lett.* **58**, 2209 (1987).
- ⁵² B. Stern, X. Ji, Y. Okawachi, A. L. Gaeta, and M. Lipson, [arXiv 1804.00357](https://arxiv.org/abs/1804.00357) (2018).